OPEN ACCESS
IOP Publishing

Plasma Sources Science and Technology

Plasma Sources Sci. Technol. **33** (2024) 015002 (16pp) https://doi.org/10.1088/1361-6595/ad171c

Atmospheric pressure plasmas interacting with wet and dry microchannels: reverse surface ionization waves

Kseniia Konina[1], Sai Raskar[2], Igor V Adamovich[2] and Mark J Kushner[3,*]

[1] Nuclear Engineering and Radiological Sciences Department, University of Michigan, 2355 Bonisteel Blvd., Ann Arbor, MI 48109-2104, United States of America
[2] Nonequilibrium Thermodynamics Laboratory, Department of Mechanical and Aerospace Engineering, The Ohio State University, Columbus, OH 43210, United States of America
[3] Electrical Engineering and Computer Science Department, University of Michigan, 1301 Beal Ave., Ann Arbor, MI 48109-2122, United States of America

E-mail: mjkush@umich.edu

Received 20 October 2023, revised 15 November 2023
Accepted for publication 19 December 2023
Published 4 January 2024

Abstract

Atmospheric pressure plasma jets (APPJs) are increasingly being used to functionalize polymers and dielectric materials for biomedical and biotechnology applications. Once such application is microfluidic labs-on-a-chip consisting of dielectric slabs with microchannel grooves hundreds of microns in width and depth. The periodic channels, an example of a complex surface, present challenges in terms of directly and uniformly exposing the surface to the plasma. In this paper, we discuss results from computational and experimental investigations of negative APPJs sustained in Ar/N_2 mixtures flowing into ambient air and incident onto a series of microchannels. Results from two-dimensional plasma hydrodynamics modeling are compared to experimental measurements of electric field and fast-camera imaging. The propagation of the plasma across dry microchannels largely consists of a sequence of surface ionization waves (SIWs) on the top ridges of the channels and bulk ionization waves (IWs) crossing over the channels. The IWs are directed into electric field enhanced vertices of the next ridge. The charging of these ridges produce reverse IWs responsible for the majority of the ionization. The propagation of the plasma across water filled microchannels evolve into hopping SIWs between the leading edges of the water channels, regions of electric enhancement due to polarization of the water. Positive, reverse IWs follow the pre-ionized path of the initial negative waves.

Keywords: atmospheric pressure plasma jets, complex surfaces, surface ionization waves, microchannels

[*] Author to whom any correspondence should be addressed.

1. Introduction

Atmospheric pressure plasmas (APPs) are used to treat solid materials to functionalize their surfaces and liquids to produce reactive species on and beneath the liquid surface [1, 2]. Technologically relevant solid surfaces treated by APPs typically do not have homogenously smooth surfaces but rather may have complex shapes and/or compositions. Such complexities include metal catalysts embedded in dielectric supports [3], wrinkled or wounded skin [4], and liquid droplets on solid materials [5]. Sources of APPs for surface treatment include dielectric barrier discharges (DBDs) [6], surface dielectric barrier discharges (SDBDs) [7] and atmospheric pressure plasma jets (APPJs) [8].

APPJs that treat surfaces typically begin as streamers that propagate as bulk ionization waves (IWs) [9]. When a bulk IW strikes a dielectric surface, the interface collects surface charge that produces a local electric field with components parallel to the surface. This local electric field then initiates and sustains the propagation of a surface ionization wave (SIW) [10]. Several recent studies have focused on the propagation of SIWs over non-planar dielectric surfaces [11–13]. In addition to charge accumulation, non-planar dielectric surfaces polarize when exposed to an electric field, which then produces electric field enhancement at locations with positive curvature and small radii [14]. This electric field enhancement can then alter further propagation of the SIWs [15].

Microfluidic devices (labs on a chip) often consist of rectangular channels, typically hundreds of microns wide and fabricated in dielectric substrates, that direct and mix liquids for analysis [16, 17]. The surfaces of microfluidic devices channels must often be functionalized to control their hydrophobicity, a process that is often performed using APPs [18, 19]. The exposed liquids in open microfluidic devices may themselves be treated by APPs for activation or chemical conversion of the fluid [20–22]. The APP treatment of these dry- and wet-channels represent another form of complex surface, albeit repetitive structures. In this regard, Patinglag *et al* produced a filamentary DBD inside a partially liquid filled microfluidic reactor containing a solution of deionized water and methylene blue, demonstrating significant reduction in the concentration of methylene blue [23]. A similar microfluidic reactor was used to demonstrate killing of *Pseudomonas aeruginosa* and *Escherichia coli* in solution [24].

APP treatment of human skin [25] also represents a topologically complex surface with channel-like features. Skin may be wrinkled with channels of hundreds of microns to more than 1 mm in depth and width [26]. These non-planar features makes it difficult to achieve uniform plasma treatment of the skin for therapeutic purposes.

In this paper, we discuss results from computational and experimental investigations of a negative APPJ sustained in Ar/N_2 flowing into ambient humid air incident onto a dielectric surface having square, 250 μm wide microchannels. The microchannels were dry and filled with water. Comparisons are made of computations to experimental fast-camera imaging of propagation of SIWs across the surface and to electric field measurements. We found that the incident bulk IW from the APPJ fills the microchannels with plasma directly under the jet while only partially filling more distant channels. The subsequent propagation of SIWs across dry microchannels is dominated by charging of the ridge of a channel which sustains a SIW. Electric field enhancement at the next ridge vertex then launches a bulk IW across the channel. The next ridge then charges, launching SIWs across the ridge and into the channel, partially filling the channel with plasma. A reverse positive bulk IW is launched from the vertex following charging. The electric field components in the SIW transition from being dominantly vertical upon initiation of the SIW to dominantly horizontal. This repetitive sequence results in the channels becoming less filled with plasma as the SIW-IW pairs propagate across the surface. The details of the propagation depend on the conductivity and permittivity of the dielectric, however the pattern does not significantly change.

Propagation of SIWs across water filled channels are dominated by increased electric field enhancement due to polarization of the high permittivity water. The end result is hopping of the SIW-IW from triple point (intersection of gas plasma, water and solid dielectric) to triple point in large part bridging the ridges of the dielectric. The majority of the charged particles in the bridges of plasma are produced by reverse IWs.

The model used in this investigation and a brief description of the experiment are in section 2. The propagation of SIWs over dry channels while varying the electrical properties of the dielectric and height of the jet are discussed in section 3. The propagation of SIWs over water-filled channels is discussed in section 4. Concluding remarks are in section 5.

2. Description of the model and experiment

2.1. Description of the model

The simulations discussed here were performed using the two-dimensional (2D) plasma hydrodynamics plasma model *nonPDPSIM*. This modeling platform is described in detail in [27] and so is only briefly described here.

nonPDPSIM is a 2D plasma hydrodynamics model executed on an unstructured mesh. Continuity equations for charged particles with the simultaneous solution of Poisson's equation are implicitly integrated in time. Fluxes for charged particles are addressed using the Scharfetter–Gummel scheme [28]. The solution of Poisson's equation takes into account surface and volumetric charging of solid materials. Surface and volumetric charging are accounted for by considering the incident flux of charged species onto surfaces, secondary electron emission by those species and by photons, and by redistribution of that charge by currents through solids having a finite conductivity. The system of equations is solved using a Newton–Raphson technique. Time steps are dynamically chosen based on not exceeding specified fractions of a Courant limited timestep and dielectric relaxation time (both of which may exceed 1), and minimizing the number of the Newton–Raphson iterations to obtain a converged solution.

After an integration timestep, continuity equations for neutral species and electron temperature are updated using the same timestep. The electron energy equation is implicitly solved using a successive-over-relaxation technique. Rate coefficients as a function of average electron energy (or electron temperature) are produced from solutions of the stationary Boltzmann's equation for the electron energy distribution. Radiation transport, photoionization and photoelectron emission are addressed using a Greens function propagator.

Neutral particle transport is addressed using a modified compressible form of Navier–Stokes (NS) equations which produces a single fluid flow field. The NS equations are reformulated in terms of number density as opposed to mass density, an approach which then better enables steep gradients in mass density at constant pressure, as may occur when a rare gas jet propagates into ambient air. Neutral species have this average advective velocity while additionally diffusing within the flow field. The steady state, stationary fluid flow field is first computed prior to applying voltage to produce the discharge.

A detailed description of the plasma-chemistry mechanism for an APPJ sustained in argon flowing into humid air is provided by Lietz *et al* [29] and Tian *et al* [30]. The mechanism includes 54 species: e, Ar, Ar($^3P_2$), Ar($^3P_1$), Ar($^3P_2$), Ar($^1P_1$), Ar(4p), Ar(4d), Ar^+, Ar_2^*, Ar_2^+, H, H^*, H^+, H^-, H_2, H_2(r), H_2(v), $H_2{}^*$, H_2^+, H_3^+, OH, OH^*, OH^+, OH^-, H_2O, H_2O(v), H_2O^+, HO_2, H_2O_2, H_3O^+, O_2, O_2(v), O_2(r), O_2^*, O_2^{**}, O_2^+, O_2^-, O_4^+, O, O^*, O^+, O_3, N_2, N_2(v), N_2(r), N_2^*, N_2^{**}, N_2^+, N_3^+, N_4^+, N, N^*, N^+. The mechanism includes about 1000 reactions. Photoionization of O_2 and H_2O results from resonance radiation from Ar(4p) and Ar(4d).

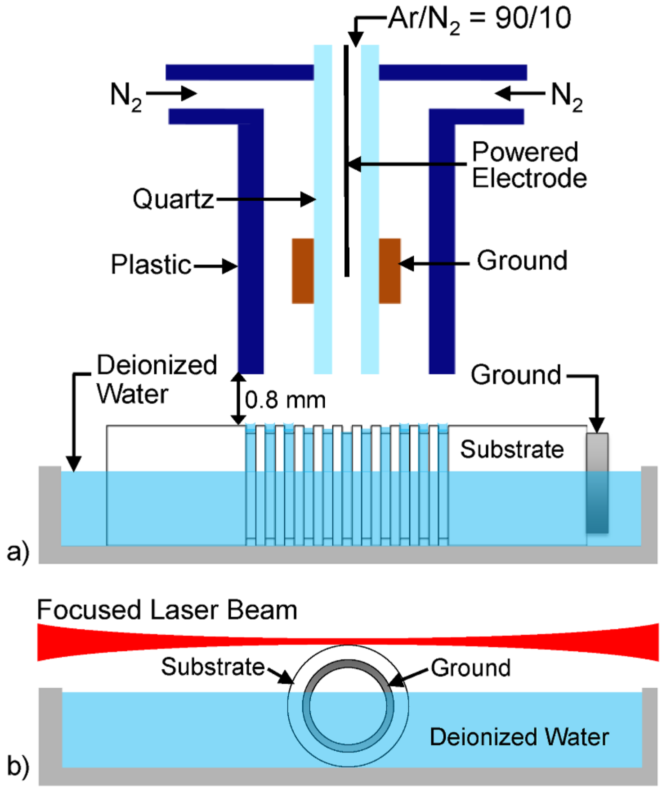

Figure 1. Schematic of the experiment. (a) APPJ over the grooved substrate sitting in a bath of deionized water. (b) Cross section showing the incident laser beam.

2.2. Description of the experiment

A schematic diagram of the experimental apparatus appears in figure 1, and is described in detail in the closely related companion paper [31]. Briefly, an APPJ (Ar/N_2 = 90/10 with a co-flow of nitrogen), sustained by high-voltage ns duration pulses, is incident on a dielectric target, placed in a Petri dish. The plasma jet is a 1 mm diameter quartz tube with a needle high voltage electrode and a grounded ring electrode, coaxial with a 10 mm diameter polycarbonate plastic tube. The flow rates of the Ar/N_2 mixture (main flow) and N_2 (co-flow) are 7 slm and 5 slm. The jet exit plane is located 0.8 mm above the target surface, a Macor ceramic tube 12.7 mm in diameter, with a series of rectangular cross section channels (0.25 mm $\times$ 0.25 mm, spanning 10 mm). A 9 mm diameter grounded electrode is inserted into the ceramic tube. The Petri dish, 10 cm diameter and 1 cm deep, is partially filled with distilled deionized water. For these conditions, the channels are filled with water due to the capillary effect. The plasma jet is powered by repetitive bursts of negative polarity ns duration pulses, 10 pulses/burst, at the pulse repetition rate of 10 kHz and burst repetition rate of 10 Hz. The pulse voltage and current waveforms are shown in [31]. The voltage waveform is approximately triangular with a full-width-half-maximum of 120 ns.

The electric field in the jet effluent was measured by ps Electric Field Enhanced Second Harmonic (EFISH) generation, discussed in detail in [31] and references therein. For the spatially resolved electric field measurements, the jet and Petri dish assembly are moved relative to the laser beam using a translation stage. The time-resolved electric field is measured by changing the delay between the discharge pulse and the laser pulse. Absolute calibration of the EFISH measurements was performed by measuring the Laplacian electric field for the same electrode and dielectric geometry. The calibration data were obtained at every measurement location, both for the vertical and horizontal components of the electric field. The spatial resolution of the diagnostic in the direction of the laser beam is quantified by traversing a pair of biased parallel cylindrical rod electrodes [31]. The calibrated EFISH signal was correlated to the peak Laplacian electric field in the gap. The diameter and position of the laser beam at the focal point are measured by scanning the beam across a knife edge. The surface curvature enables placing the laser beam close to the surface ($\approx$70 μm), without clipping.

3. Propagation of APPJs across dry microchannels

A schematic of the computational geometry is in figure 2. The coordinate system is Cartesian with the left edge using reflective boundary conditions. The depth of the domain is 2.35 mm. The jet consists of a powered blade electrode 1 mm wide having a tip with a 0.5 mm radius of curvature. The electrode is centered in a tube (the central nozzle) having an inner width of 2 mm and wall thickness of 0.5 mm. A grounded electrode surrounds the inner tube at the height of the tip of the electrode. An Ar/N_2 mixture with humid air impurities

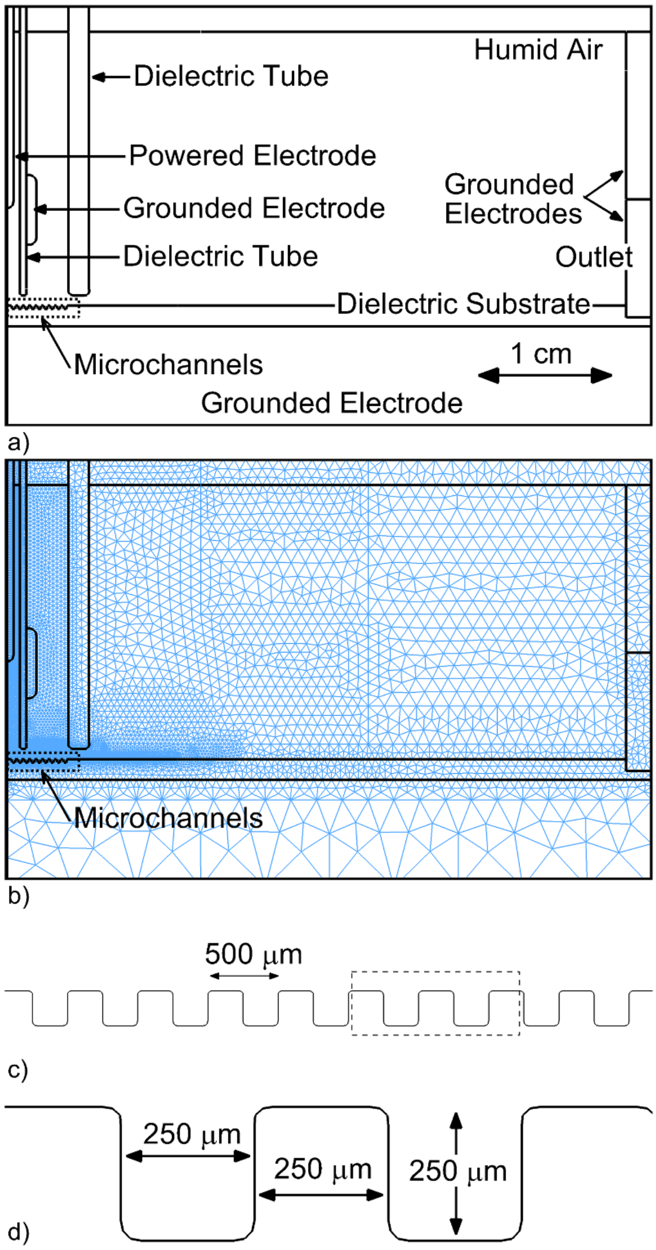

Figure 2. Schematic of the computational geometry. (a) Full computational domain, (b) computational mesh, (c) enlargement showing chain of microchannels (dotted domain in previous images), and (d) enlargement of individual channels.

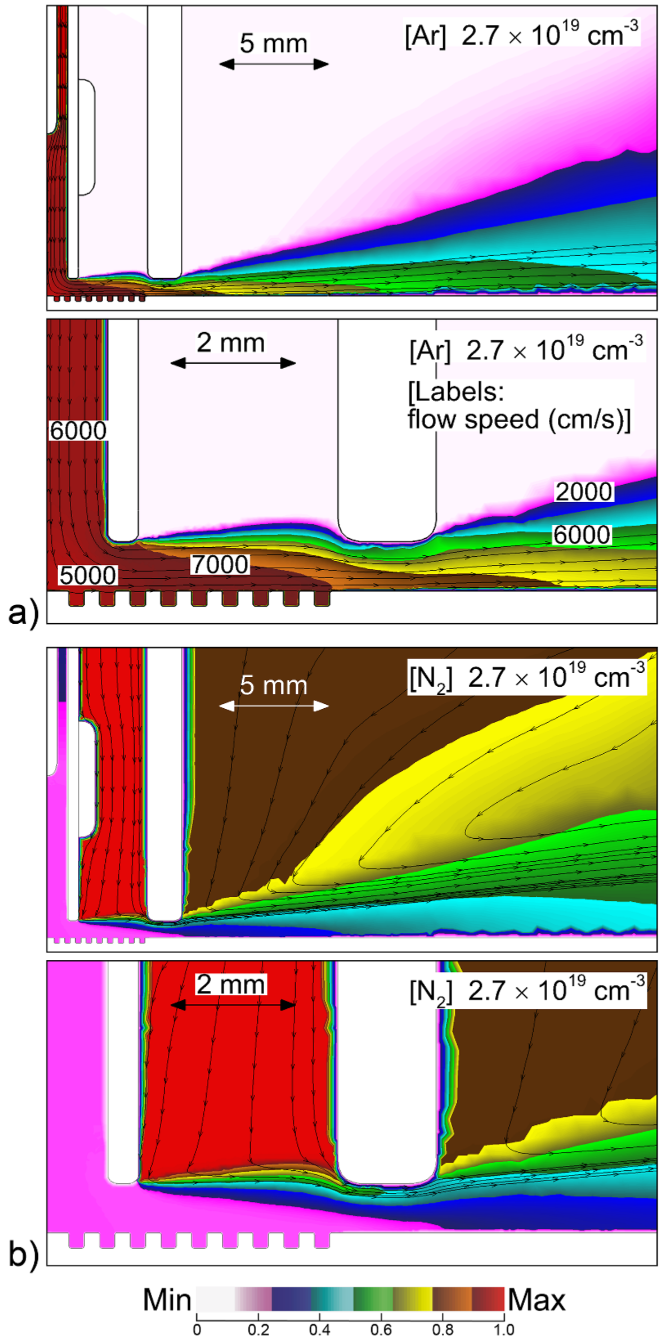

Figure 3. The stabilized fluid flow field with flow streamlines prior to application of the voltage pulse. The streamline are labeled with speeds (cm s^{-1}). (a) Argon and (b) N_2 flow with enlargement near the channels.

($Ar/N_2/O_2/H_2O = 0.9/0.1/10^{-5}/10^{-5}$) flows through the central nozzle at 7 lpm. A nitrogen shield gas is flowed at 1.2 lpm through a channel surrounding the central nozzle having a width of 1.4 mm. The relative dielectric permittivity of the inner and outer tubes is $\varepsilon_r = 4$. The gases flow into ambient air with a humidity 0.5%. Humid air is injected at the rate of 10 lpm from the top boundary of the domain to minimize stagnation zones and to mimic entrainment of room air by the jet. Gas is exhausted through pump ports on the right edge of the domain.

The substrate is located 0.8 mm beneath the edge of the tube and 7.5 mm below the tip of the electrode. The relative dielectric permittivity of the substrate in the base case is $\varepsilon_r = 6$. A series of 8 microchannels are in the substrate having a spacing, width and depth of 250 μm, as shown in figure 2. The electrical ground plane is located under the 1.5 mm thick substrate and also wraps around the domain. The voltage pulse applied to the powered electrode has an amplitude of −25 kV with a rise time of 5 ns, pulse length of 25 ns and fall time of 5 ns.

The initial neutral gas flow field is shown in figure 3. The boundary layer of argon over the microchannels is

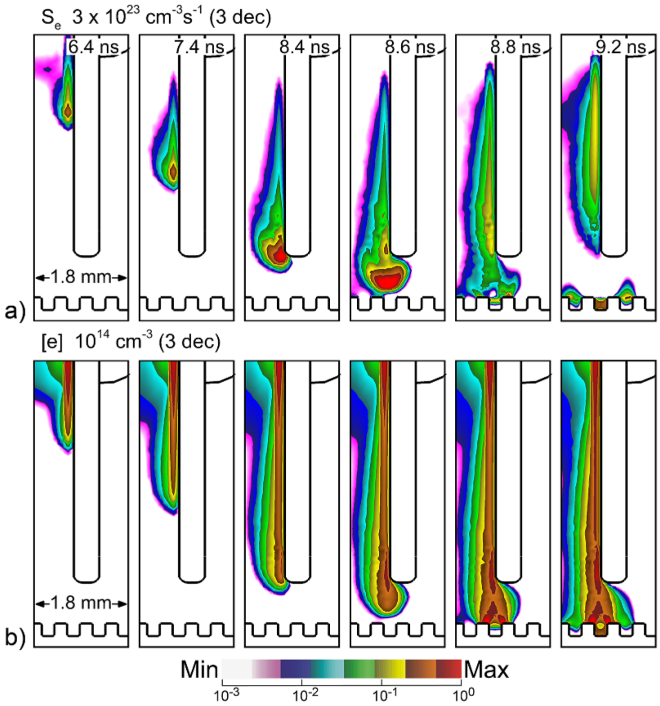

Figure 4. Ionization wave propagation through the tube and onto the channeled substrate. (a) Electron impact ionization source (cm^{-3} s^{-1}) and (b) electron density (cm^{-3}). Images are plotted on a 3-decade log scale with maximum values indicated in each frame.

approximately 1 mm thick with there being minimal penetration of the N_2 shield gas. The plasma is largely confined to the argon dominated central flow and boundary layer.

The experiment has 3D characteristics that will not be captured in our 2D model, and so approximations and scaling need to be applied. The experimental device is a cylindrical plasma jet incident onto a grooved cylinder whose axis is perpendicular to that of the jet. To capture the critical phenomena, the simulations were performed in Cartesian coordinates that best represents the propagation of SIW along the surface of the grooved cylinder. One of the consequences of using Cartesian coordinates is that the powered electrode is a blade in the simulation instead of a pin in the experiment. This difference in geometry results in less geometrical electric field enhancement, both at the physical surface of the electrode and at the leading edge of the bulk IWs in the gas phase. To obtain comparable IW characteristics then requires higher voltage magnitudes in a Cartesian geometry compared to cylindrical. Based on past experience, voltage amplitudes should be 1.5–2 times as large in Cartesian simulations [32]. This higher voltage then produces higher propagation speeds of the SIW.

The propagation of the IW from the tube to the substrate is shown in figure 4. The simulation begins with a small spot of plasma (1×10^{11} cm^{-3}, 0.3 mm diameter) placed at the tip of the powered electrode. This initial spot of plasma enables launching of an IW towards the wall of the tube. (A sensitivity study was also performed on the influence of a uniform background pre-ionization density of 10^5–10^7 cm^{-3}. The results of the simulation were insensitive to this level of uniform pre-ionization.) The IW is directed by the applied electric field between the powered electrode and the grounded electrode surrounding the tube. When the IW strikes and charges the inner surface of the tube, a SIW is produced, which then propagates along the tube in a *surface-hugging* mode [33]. The ionization source in the head of the SIW is maximum at 2–3 $\times$ 10^{23} cm^{-3} s^{-1}, with a propagation speed of 1.3×10^8 cm s^{-1} [34, 35]. The electron density produced by the SIW is 3–4 $\times$ 10^{13} cm^{-3}, and is 300–400 μm thick along the wall.

When the SIW reaches the end of the tube, a bulk IW is launched across the gap. When the IW reaches within a few hundred microns of the surface, polarization of the dielectric and geometrical electric field enhancement direct the IW towards the edges of the ridges of the microchannels. Upon application of full voltage, the electric field at the vertex of the channel under the nozzle is 5.0 kV cm^{-1} ($E/N = 20.5$ Td, 1 Td $= 10^{-17}$ V cm^2). As the IW wave approaches the surface, voltage is compressed in front of the lengthening conductive plasma column, momentarily increasing the electric field at the vertex to 64 kV cm^{-1} (260 Td) at 8.4 ns. The IW intersects the dielectric at about 8.7 ns.

The electron impact ionization source, electron density and E/N are shown in figure 5 upon intersection of the IW with the chain of microchannels and propagation across the channels. When the IW reaches the surface, the applied electric field is largely vertically oriented, which enables penetration of the plasma into the channels (adjacent to location 1). With a fully planar surface, intersection of the IW with the dielectric surface charges the surface, producing an electric field component parallel to the surface which launches a SIW. With fully planar surfaces, as the surface charges, the local electric field is reoriented to be more perpendicular to the surface, with the SIW being sustained by space charge in the head of the IW [36]. In the case of the rectangular microchannels, geometrical electric field enhancement occurs at the vertex of the ridges of the channels which directs the incoming IW to those locations. Charging of the vertex produces electric components horizontally along the top ridge of the channel and vertically along the inside surface of the channel, for example, at ridge 2. A SIW then propagates along the top of the ridge and down the side of the channel. The latter contributes to filling the channel with plasma. The maximum electron densities across the top of the ridges are 10^{14} cm^{-3}.

As the SIW propagates along the ridge of the channel, the surface is charged. This charging reduces the electric field enhancement at the edges. When the SIW reaches the right edge of the ridge, the vertex across the channel is largely uncharged and so retains its geometrical electric field enhancement. This electric field enhancement directs the SIW across the channel, now as a bulk IW, to intersect the opposite vertex. Prior to arrival of the IW, the electric field at the vertex of ridge 4 is 88 kV cm^{-1} (300 Td). Upon intersection of the IW with the vertex, the surface of the vertex is charged, launching a SIW along the top of the next ridge and down the adjacent right side wall into the channel. This launching of the IW across the channel leaves the left side of the channel initially without coverage by plasma. This process of propagation

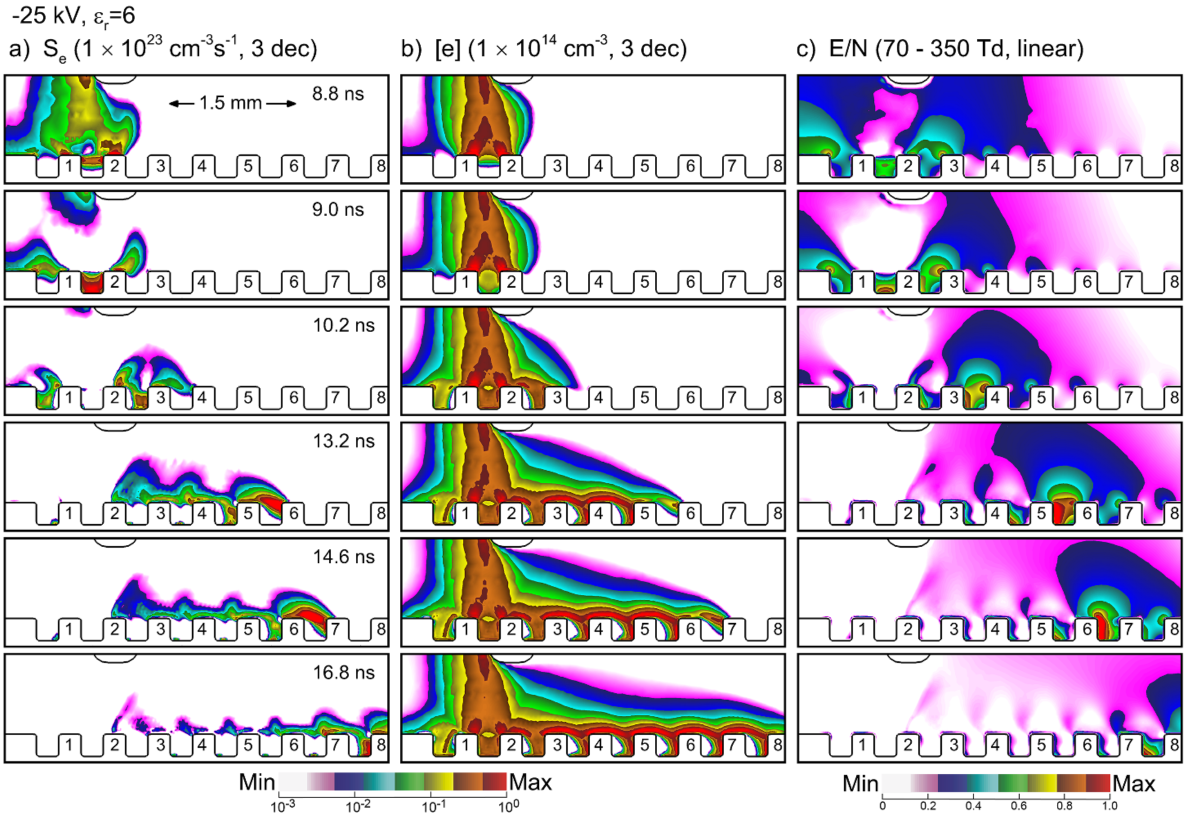

Figure 5. Surface ionization wave propagation across a chain of microchannels for the base case. (a) S_e, electron impact ionization source (cm^{-3} s^{-1}, 3-decade log scale). (b) [e], electron density (cm^{-3}, 3-decade log scale). (c) E/N, reduced electric field (Td, linear scale). Maximum values or the range of values are noted in the images.

of the SIW across the top of the ridge and launching an IW across the channel into the vertex of the next ridge continues from one microchannel to the next. That portion of the microchannel that is not covered by plasma increases as successive microchannels are encountered.

The electron impact ionization source and electron density during the propagation of the SIW and launching of the IW across the channel are shown enlarged with finer time resolution in figure 6. The character of the IW, negative or positive, is determined by the space charge at the leading edge of the IW. A negative IW will have negative space charge and generally propagates left-to-right in this geometry. A positive IW will have positive space charge and generally propagates right-to-left. The direction of propagation and character of the IW are indicated by N (negative) and P (positive) labels in figure 6. At 12.5 ns, the SIWs on the top ridge and inner wall are both negative. With this being a negative IW (for propagation left-to-right in the figure), there is a small diffusion flux ahead of the ionization front. Although photoionization is not required for propagation of the negative IW, there is nevertheless photoionization that occurs ahead of the ionization front. The combination of the electron diffusion flux and photoionization seeds electrons in the high electric field region at the vertex of the next ridge, though the diffusion flux dominates for these conditions. These seed electrons then launch a positive IW propagating from right-to-left across the channel. The reverse positive IW is responsible for the majority of the plasma density across the channel. This reverse wave extends back to the ridge of the prior channel, producing a positive SIW across the ridge. The end results is a curvature in the plasma density that extends from vertex-to-vertex of the ridges of the microchannels.

Conventional positive IWs propagating into non-ionized gases require a source of seed electrons ahead of the IW to sustain propagation. These seed electrons are typically provided by photoionization. The reverse, positive IWs produced here occur independent of including or excluding photoionization. This insensitivity to photoionization results from the reverse, positive IWs propagating through the previously ionized channels that were formed by the forward negative IW. As a result, photoionization is not needed to sustain the positive IW. This is a similar situation to the reverse IW that is produced in a dielectric barrier discharge sustained with unipolar, square wave voltage pulses. The reverse IW that occurs on the downward edge of the voltage pulse propagates through the pre-ionized channel produced by the forward wave.

Marskar and Meyer [11] performed similar simulations for propagation of positive IWs in air over square channels having sizes $\geqslant$500 μm. They also observed a hopping of the SIW across channels with the channels under the electrode more filled with plasma. The inner surfaces of more distant channels were less covered by plasma, as seen here. With their simulations addressing initially positive waves, their propagation properties were in general more sensitive to photoionization, and particularly to the transparency of the channels. For

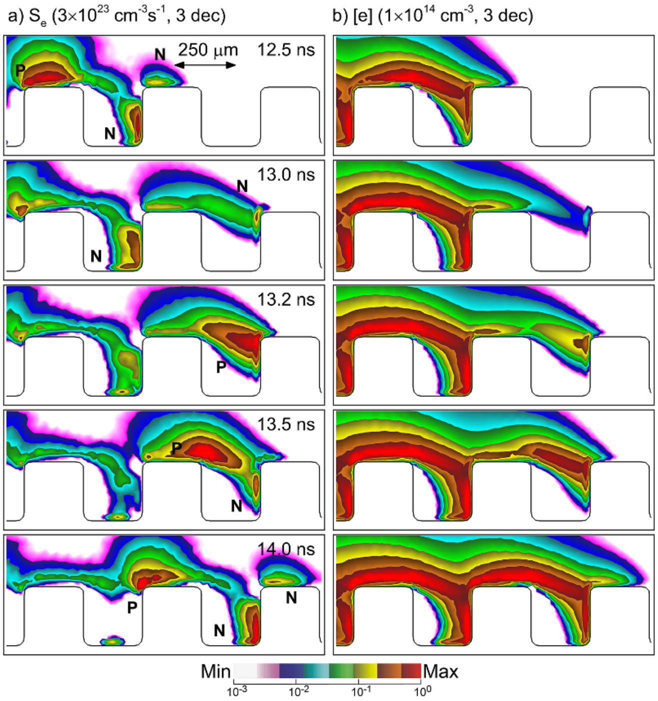

Figure 6. Plasma properties demonstrating reverse (positive) ionization wave. (a) S_e, electron impact ionization source (cm^{-3} s^{-1}) and [e], electron density (cm^{-3} s^{-1}). The 'N' and 'P' labels indicate a negative or positive ionization wave. Images are plotted on a 3-decade log scale with maximum values indicated.

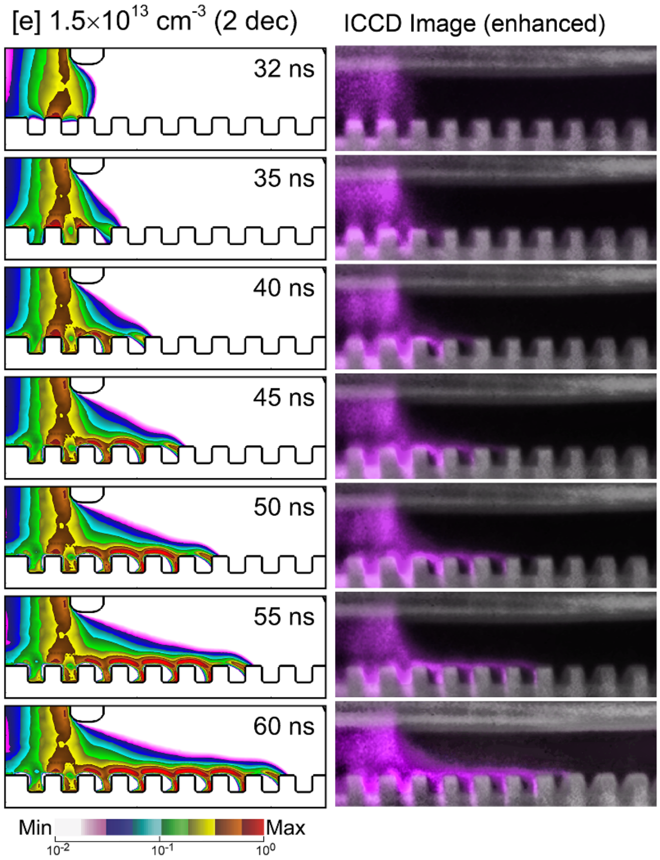

Figure 7. Comparison of (left) simulated electron density for applied voltage of −18 kV with (right) ICCD imaging for the plasma jet propagating along dry microchannels. The ICCD imaging frames were chosen for times that showed similar structure as the simulations. The ICCD images have been enhanced emphasize regions of weak emission.

the initially negative waves discussed here, the general trends were fairly independent of including or excluding photoionization or initializing with a low background electron density as might be expected with negative waves. The exception is that the initially negative SIWs propagated more rapidly when including photoionization.

Experimental validation of the predicted interaction of the negative plasma jet with microchannels comes from comparison of the electron density obtained from the simulation with imaging of optical emission using a fast intensified charge-coupled device (ICCD) camera, shown in figure 7. For these comparisons, the applied voltage in the simulation is −18 kV. The plasma density is shown on a 2-decade log-scale to facilitate better comparison to the estimated dynamic range of the ICCD images. The ICCD images have been artificially enhanced to emphasize regions of weak optical emission. The times shown for the simulation results were chosen to align with the available ICCD images.

In general, the qualitative features of IW propagation across the microchannels shown by the ICCD imaging are reproduced by the simulation. These features include the filling of the microchannels with plasma directly under the plasma tube; lack of direct plasma exposure of the inner wall of the microchannels which worsens with propagation of the plasma across the microchannels; focusing of the IW into the vertex of following microchannels; and the curvature of the plasma. Although not readily apparent in the images selected here, finer time resolution of the ICCD images confirm the backwards, positive IW that bridges the microchannels.

Other validation of the IW dynamics comes from comparison of electric field measurements using the EFISH technique. Predicted and measured electric fields are shown in figure 8 at 75 μm above and centered on the top ridges of the channel. These comparisons should be evaluated on the basis of qualitative agreement with trends and not absolute quantitative agreement due to differences between the 3D configuration for the experiments and 2D model. The experimental measurements average the EFISH signal over the spot-size of the laser whereas the simulations are at a single point, which produces a larger value of the electric field.

There is general agreement between the trends of the experiments and simulations. The increase in axial electric field (E_y) during 20 ns to 30 ns corresponds to the approach of the bulk IW towards the surface. With the trailing plasma column being highly conductivity and which cannot support a significant electric field, voltage is compressed in front of the IW. This compression produces an increase in E_y at the surface. There is little, if any, lateral (E_x) electric field at this time. When the IW arrives at the surface at 30 ns, the E_y collapses from its peak of nearly 50 kV cm^{-1} due to charging of the dielectric. Directly under the plasma jet, the lateral E_x component of the electric field remains small. At this time, the axial E_y electric field

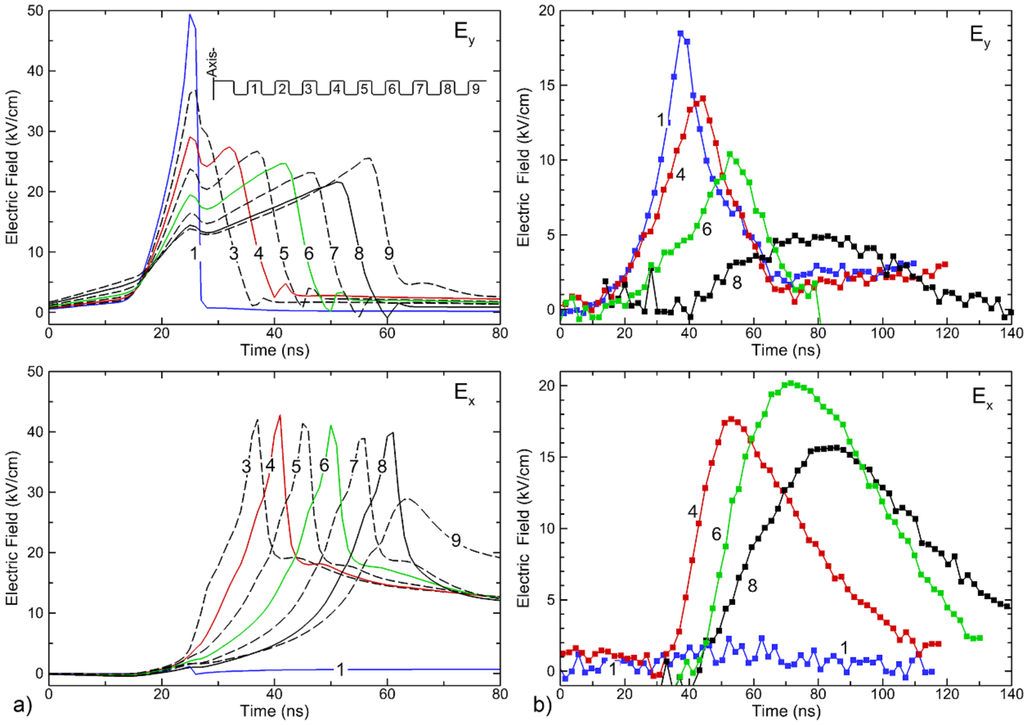

Figure 8. Comparison of electric fields on the top of ridges of the channels numbered according to the schematic. (a) Simulation and (b) EFISH measurements. The channels in the simulated results that correspond to the experiment are shown with solid lines.

at the outer microchannels decrease with distance reflecting the larger distance from the electrode. As the IW propagates across the microchannels, the axial electric field E_y increases before collapsing. The increase is due to the approaching IW which has some height above the surface and so produces an axial field. When the IW finally reaches the ridge, the surface is charged and E_y collapses.

The peak of the lateral E_x electric field generally follows in time the peak of the axial electric field E_y. The axial E_y electric field is in large part reduced by charging of the dielectric, which then enables generation of the lateral E_x component. With the plasma column extending from the cathode to the dielectric, a large fraction of the cathode potential is conducted towards the surface. For a cathode potential of -18 kV, the potential immediately above the surface under the jet is as large as -12 kV. This transferred potential then induces a lateral electric field which is intensified in the head of the SIW. The maximum in the lateral components E_x are delayed in time for the more distant channels as that maximum occurs when the SIW arrives.

3.1. Voltage

The electron density during propagation across the microchannels is shown in figure 9 for voltages of -20 kV, -22.5 kV, and -25 kV with a voltage rise time of 5 ns. The speed of propagation of the IW increases with voltage, from 1.0×10^7 cm s^{-1} for -18 kV (shown in figure 7) to 4.0×10^7 cm s^{-1} for -25 kV. There are commensurate increases in electron density, from 1.5×10^{13} cm^{-3} for -18 kV to 1.0×10^{14} cm^{-3} for -25 kV. Although these trends for increasing speed and electron density are expected with an increase in voltage, the relative increases are smaller than expected based on analogies for propagation across flat surfaces. Propagation of the SIW across the channels is maintained by electric field enhancement at the vertices of the ridges, and this occurs in a repetitive and periodic manner. Prior to arrival of the SIW at, for example, ridge 5 in the center of the array, E/N at the vertex exceeds 150 Td even for the lowest voltage. This value of E/N is well above that found in the head of bulk IWs sustained in argon. These vertex enhanced values of E/N results in rapid avalanching both in the forward and reverse IWs. This geometrical enhancement, aided by polarization of the dielectric, then negates at least part of the need for higher voltages to sustain the SIW. The end result is that the propagation is not as sensitive to voltage as would be a bulk IW or a SIW over a flat surface.

3.2. Dielectric permittivity

The permittivity of the dielectric determines, in part, the electrical capacitance of the substrate. The general trends expected for propagation of a SIW across flat substrates is that the speed of the wave will decrease with increasing relative permittivity, ε_r. The increase in ε_r produces an increase in surface capacitance, C_S (F cm^{-2}). Increasing capacitance requires more net current from the SIW onto the surface to charge that capacitance, thereby lengthening the dwell time of the SIW at any given location. These principles were experimentally quantified by Morsell *et al* [37]. With the microchannel geometry, in addition to the bulk value of ε_r, the local value of C_S varies due to the local geometry. Dielectrics that are thicker (surface is a

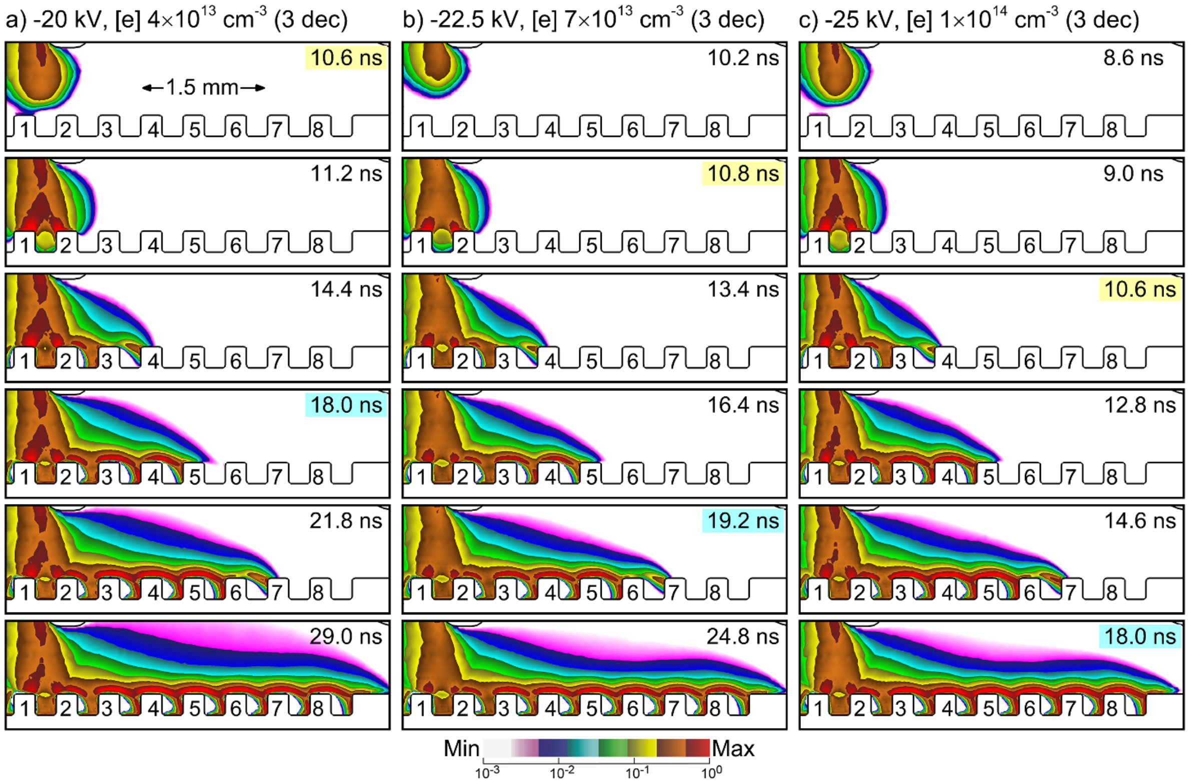

Figure 9. Electron density during surface ionization wave propagation across a chain of microchannels for different voltages for otherwise the base case conditions. (a) −20 kV, (b) −22.5 kV and (c) −25 kV. The time for the image is noted in each frame. The horizontally aligned images are for the same propagation distance. The shaded times indicate images at approximately the same time. Densities are plotted on a 3-decade log scale with the maximum value noted.

greater distance from the ground plane) will have smaller values of C_S. Surface locations with smaller radius of curvature will have larger values of C_S. With the substrate being 1.5 mm thick and the channel height being 250 μm, the local value of C_S varies from 3.54 pF cm^{-2} to 4.25 pF cm^{-2} for the base case value of $\varepsilon_r = 6$. The effective capacitance at the vertex of the channels is about 20 pF cm^{-2}. If the SIW followed the contours of the surface into and out of channels, we might expect the SIW to speed-up and slow down as regions of smaller and large values of C_S are encountered. With the SIW not being conformal to the ridges and channels, there is some spatial averaging of capacitance of the surface as the SIW passes over these structures.

The electron densities of SIWs passing over the channels for relative permittivity of the substrate of ε_r, = 2, 6 and 20 are shown in figure 10. The bulk IW arrives onto the substrate earlier for high permittivity materials due to polarization of the substrate. High permittivity materials push potential into bounding materials of lower permittivity, such as the gas above it, which then increases the bulk electric field and accelerates the bulk IW. With the substrate being only 1.5 mm thick and the substrate-to-electrode distance being about 1 cm, the increase in bulk electric field resulting from polarization of the substrate is not large. The arrival of the bulk IW onto the surfaces is shortened by only about 0.5 ns with ε_r, increasing from 2 to 20.

The earlier arrival of the bulk IW for larger ε_r is negated by the slower propagation of the SIW across the microchannels having larger permittivity. For example, the propagation speed from the ridge of channel 3 to the ridge of channel 8 for $\varepsilon_r = 2$ is about 5.7 × 10^7 cm s^{-1}. For $\varepsilon_r = 20$, the speed is 1.9 × 10^7 cm s^{-1}. Due to this increase in dwell time with more current flowing onto the surface to charge a larger capacitance, the maximum electron density increases from 8 × 10^{13} cm^{-3} for ε_r = 2–2 × 10^{14} cm^{-3} for $\varepsilon_r = 20$. The SIWs across the high permittivity channels are more conformal to the surface with less filling of the channels. Lower permittivity with shorter charging time afford more opportunity for SIWs to propagate along the inside surfaces of the channels.

In the simulations of Marskar and Meyer [11], the speed of propagation of their positive SIW increased with increasing permittivity of the substrate, whereas our results (for a negative wave) show that the speed of the SIW decreases. These different trends are, in fact, consistent with the plasma-dielectric synergies, and the polarization of the dielectric. In Marskar and Meyer, the gap between the tip of the electrode and substrate was 2 mm, whereas the thickness of the dielectric was 5 mm. Assuming flat surfaces, increasing permittivity from $\varepsilon_r = 3$ to $\varepsilon_r = 9$ for their dimensions increases the electric field in the gap by a factor of 1.43. This increase in voltage dominates in increasing propagation speed over the increase in capacitance which would otherwise slow the wave speed. For our conditions, the increase in electric field in the gap when increasing permittivity from $\varepsilon_r = 3$ to $\varepsilon_r = 9$ is only 1.04, and so the slowing of the SIW due to the increase capacitance dominates.

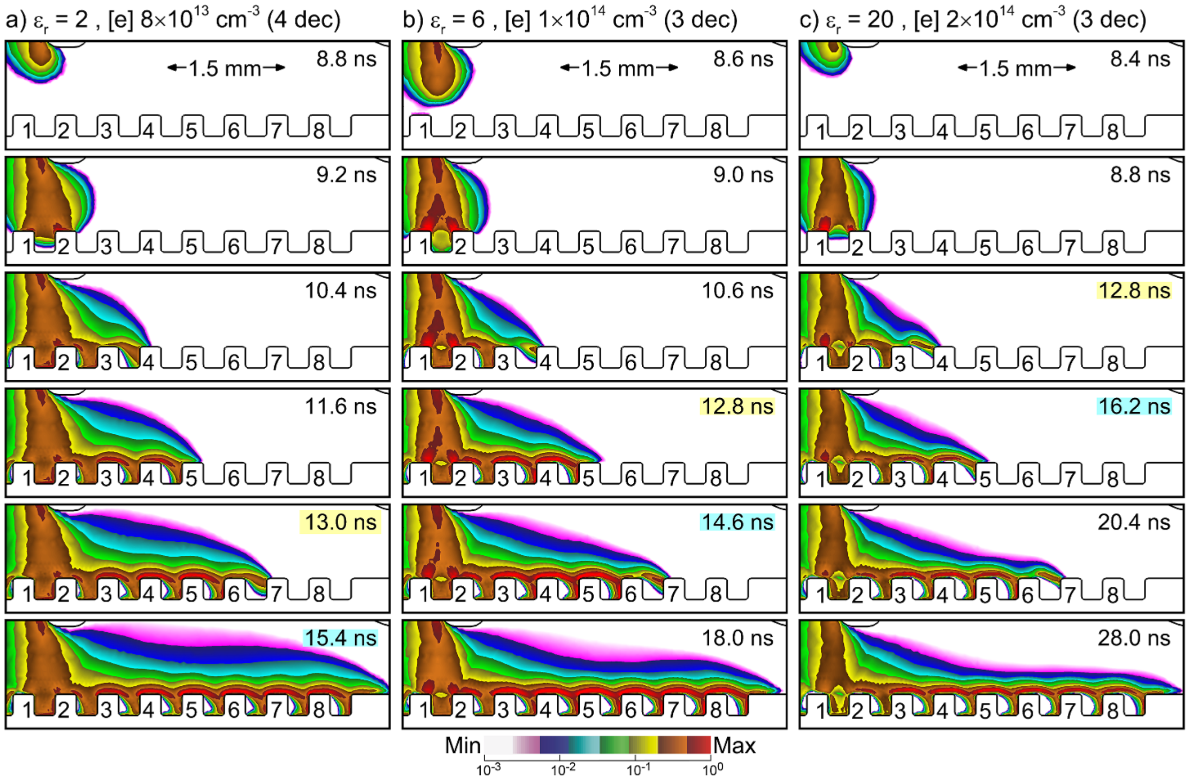

Figure 10. Electron density during SIW propagation across a chain of microchannels for different permittivity of the substrate for otherwise the base case conditions. (a) $\varepsilon_r = 2$, (b) $\varepsilon_r = 6$ and (c) $\varepsilon_r = 20$. The time for the image is noted in each frame. The horizontally aligned images are for the approximately the same propagation distance. The shaded times indicate images at approximately the same time. Densities are plotted on a 3-decade log scale with the maximum value noted.

3.3. Conductivity

The conductivity of the dielectric substrates of interest to biotechnology and chemical conversion will likely be small and support small, if not negligible, current densities through the material. That said, conductivity of the substrate is a possible control parameter for the coverage of the surface and speed of propagation of the SIW. In the absence of significant bulk conductivity of the dielectric, current continuity through the dielectric is maintained by displacement current with charging limited to the surfaces of the dielectric. With increasing conductivity of the dielectric, current continuity is progressively maintained by conduction current through the dielectric which depletes surface charge and decreases the potential drop across the dielectric. The latter trend results in more voltage being dropped across the bulk plasma while decreasing the parallel components of electric field at the surface. In the extreme case of an ideal metal substrate, all of the voltage remains in the gap (or other non-zero impedances in the circuit) and there is no parallel component of the electric field at the surface.

The electron densities during propagation of the SIW across channels having conductivities of $\sigma = 0$–10^{-3} S cm^{-1} are shown in figure 11. These values of conductivities were chosen so that the dielectric relaxation times ($\tau = \varepsilon/\sigma$) scale from infinite (no conductivity) to being commensurate with the time required for the SIW to propagate across several channels (a few ns). Similar to increasing permittivity, the increase in conductivity decreases the speed of propagation of the SIW across the channels. The value of τ is the characteristic time below which current through the material is dominated by displacement current (surface charging) and above which conduction current (charge transport through the material) dominates. For all conductivities, the SIW begins propagating laterally across the channels. However, for the non-zero conductivities, the propagation stalls at some point. This stalling occurs at 32 ns for $\sigma = 2 \times 10^{-4}$ S cm^{-1} ($\tau = 2.7$ ns) at the 7th channel, and at 19 ns for $\sigma = 10^{-3}$ S cm^{-1} ($\tau = 0.53$ ns) at the 4th channel.

Current continuity from the powered electrode to the ground plane through the substrate is maintained by a combination of displacement and conduction current. In the base case having $\sigma = 0$, after the bulk IW reaches the dielectric, current to the surface of the dielectric is largely delivered by conduction. Displacement current through the substrate completes the circuit and maintains current continuity. Upon charging the underlying dielectric to the available voltage, the local impedance of the dielectric increases and the displacement current is greatly diminished. In order to maintain current continuity, the SIW extends to uncharged surfaces of the dielectric that have a lower impedance and which are able to pass displacement current to ground. For zero conductivity, as long as current is flowing through the plasma, the SIW must continue to expand to seek out uncharged surfaces that support displacement current to complete the circuit.

With increasing conductivity of the dielectric, a larger fraction of the current continuity can be maintained by conduction

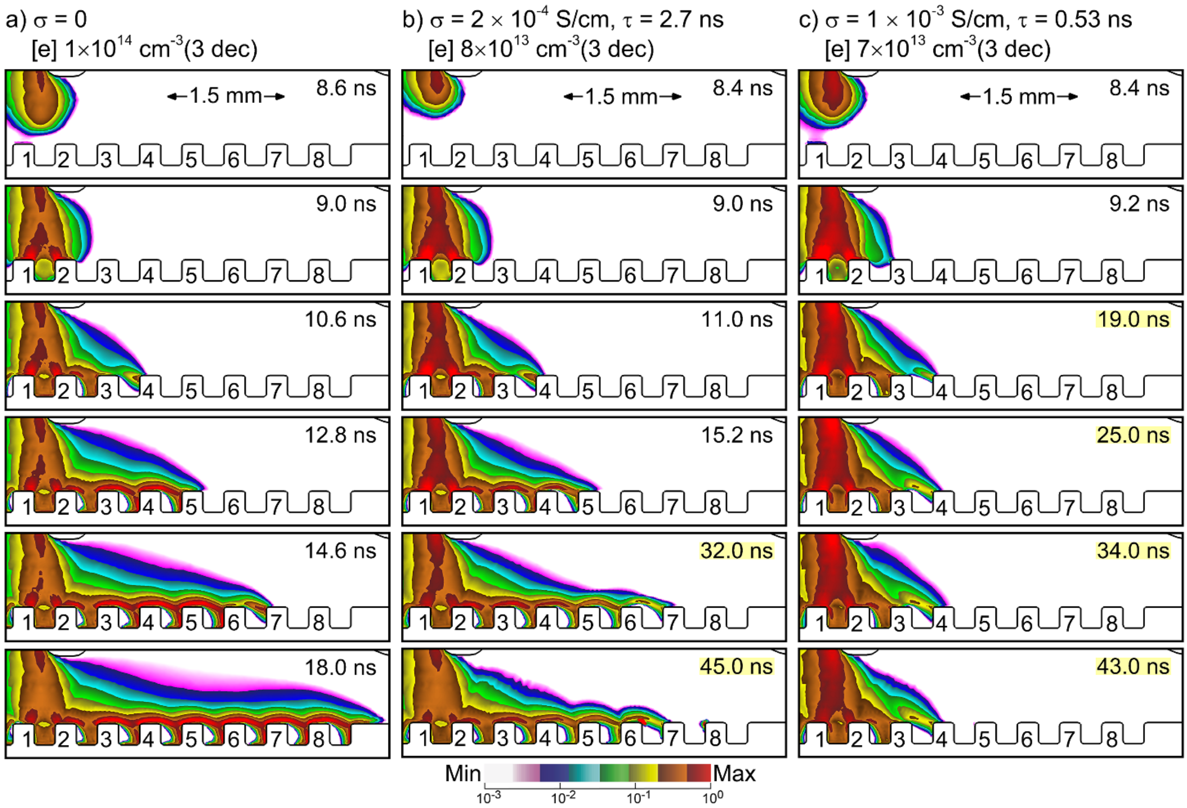

Figure 11. Electron density during SIW propagation across a chain of microchannels for different conductivities, σ, and dielectric relaxation times, τ, of the substrate for otherwise the base case conditions. (a) $\sigma = 0$, (b) $\sigma = 2 \times 10^{-4}$ S cm^{-1}, $\tau = 2.7$ ns, and (c) $\sigma = 1 \times 10^{-3}$ S cm^{-1}, $\tau = 0.53$ ns. The time for the image is noted in each frame. The horizontally aligned images are for the approximately the same propagation distance of the SIW. The shaded times indicate when the propagation of the SIW stalls. Densities are plotted on a 3-decade log scale with the maximum value noted.

through the dielectric. Unlike displacement current that terminates when the local capacitance is charged, the conduction current can, in principle, continuously flow, particularly if the substrate functions as the anode. When the SIW expands to the point that current continuity is maintained by conduction current, the SIW will stall. At this point, there is no need for further expansion of the SIW to find a lower impedance to pass displacement current. Here, the distance of propagation at which the SIW stalls decreases with increasing conductivity. Again, in the limit that the substrate is an ideal metal, there would be little if any expansion of the SIW.

This explanation should also apply to flat surfaces. The nuance with a surface composed of microchannels (or any structured surface) is that geometrical electric field enhancement and polarization focus current into sub-regions of the surface. This focusing of current, which locally charges the dielectric, to some degree limits the total current flow. To maintain current continuity, the plasma launches new bulk ionizations waves. By virtue of their transient nature, these newly launched waves also add bursts of displacement current connecting the head of the IW to uncharged dielectric ahead of the IW. This need to seek uncharged dielectric to maintain current continuity is manifested in the hopping of the SIW across the surface.

3.4. Height of the pin electrode

The height of the electrode above the substrate, d, and gap between the nozzle and substrate, h, affect SIW propagation across the microchannels in at least two modes. The first is gas dynamics, which is a function of h. The purpose of the N_2 shielding gas is to minimize the influence of oxygen and water vapor from the ambient on the propagation of SIW. Smaller gas gaps h accomplish this isolation. However, the close proximity of the shield gas to the argon boundary layer also increases the penetration of N_2 into the boundary layer. Larger gaps h increase the thickness of the argon dominated boundary layer while decreasing the penetration of N_2 into the boundary layer. The second mode is the applied E/N, which is a function of d. Larger heights of the electrode reduce the applied E/N which lowers the speed of propagation of the initial bulk IW wave and which extends to the SIW.

The electron density during propagation of the bulk IW and SIW across the microchannels is shown in figure 12 for electrode heights and gas gap heights of d = 7.5–9 mm, and h = 0.8–2.3 mm. This was accomplished by translating the entire jet assembly upwards. The arrival of the bulk IW onto the surface is only moderately delayed by the increase in electrode height. For d = 7.5 mm, the IW arrives at 8.7 ns while for d = 9 mm, the IW arrives at 10.1 ns. Once the SIW is established, this early arrival translates

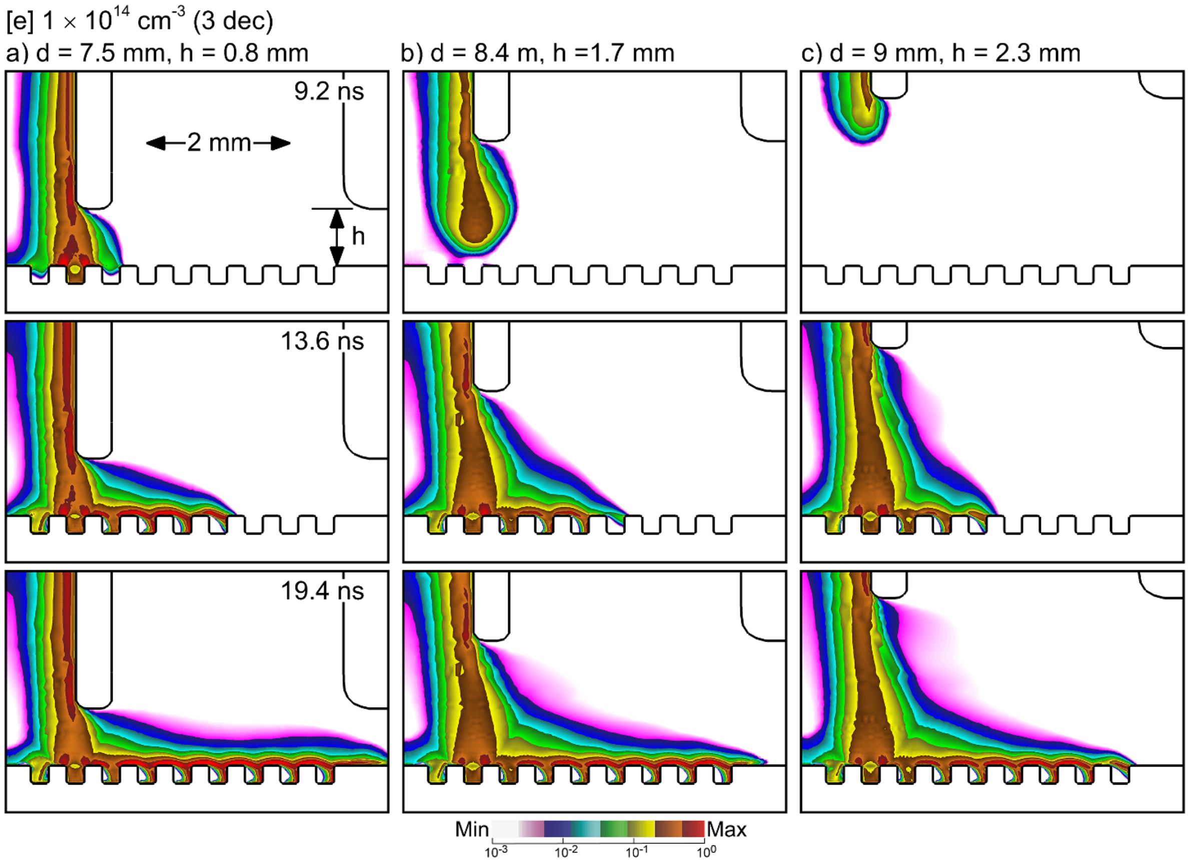

Figure 12. Electron density during surface ionization wave propagation across a chain of microchannels for different heights of the powered electrode above the substrate. The electrode position above the electrode is d. The gap between the substrate and bottom of the nozzle is h. (a) $d = 7.5$ mm, $h = 0.8$ mm, (b) $d = 8.4$ mm, $h = 1.7$ cm and (c) $d = 9.0$ mm, $h = 2.3$ mm. Densities are plotted on a 3-decade log scale with the maximum value noted.

into higher propagation speeds across the microchannels. For $d = 7.5$ mm, the SIW propagates with a lateral speed of 4.0×10^7 cm s^{-1} across the last four channels, while for $d = 9$ mm, the speed is 3.4×10^7 cm s^{-1}. The larger gap having less N_2 in the boundary layer produces a SIW that is thicker, penetrating deeper into the argon dominated boundary layer.

4. Propagation of APPJs across water filled microchannels

Plasma interactions with small individual volumes of liquids can be particularly efficient in terms of activating the liquid due to the high surface-to-volume ratio. Large throughputs of plasma activated liquid is then accomplished using parallel processing. The combined use of plasma activation of liquids flowing through microfluidic labs-on-a-chip provides the opportunity to manipulate, mix and utilize the activated liquid in a controllable manner, and provides the opportunity to parallel process. During propagation of plasma jet induced SIWs across dry channels, there are symbiotic interactions between the dielectric and the propagating SIW. We expect those interactions to extend to water filled channels. In this investigation, we are focused on how water filled channels effects propagation of the SIW, and so the water is modeled as a dielectric having a permittivity of $\varepsilon_r = 80$.

Our intent is to compare results of the simulations to companion experiments. The experimental arrangement with gas flow and open channels resulted in the water in channels directly under the jet to be emptied or depleted of water. The levels of and shape of the meniscus of the water in individual channels shown by imaging was approximated in the numerical mesh.

Simulated plasma properties are shown in figure 13 for the SIW propagating across water filled channels; electron impact ionization source (S_e), electron density (n_e), and reduced electric field (E/N). The intersection of the dielectric substrate, water and gas resembles a triple point [38] at which electric field enhancement occurs. Polarization of the water having a meniscus that is concave down would normally locally reduce the electric field in the channels under the nozzle. However, the expulsion of potential out of the wet channels by the high permittivity of the water produces a net increase in electric field at the surface of the water. The transition of the meniscus to convex up in channels further from the nozzle combined with polarization of the water results in locally increasing the electric field, enhanced by the expulsion of potential out of the high permittivity water. The combination of triple point

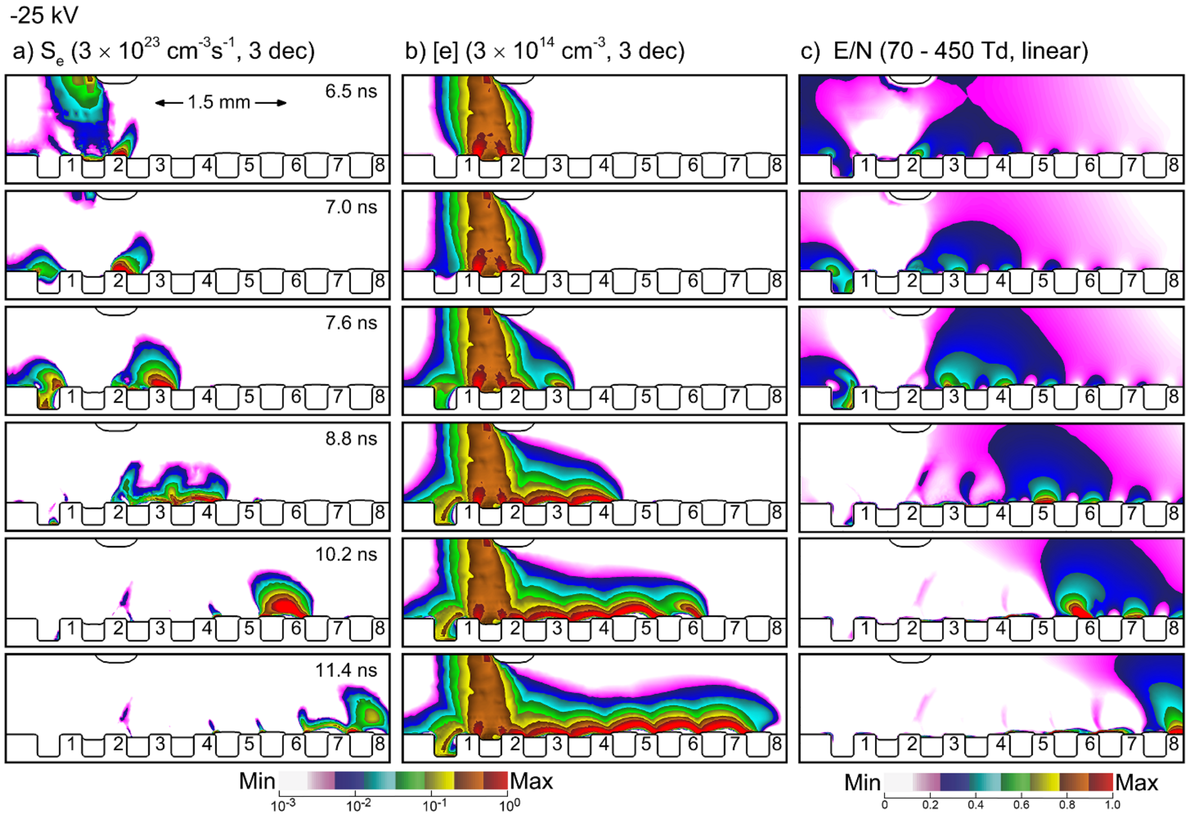

Figure 13. Surface ionization wave propagating across a chain of wet microchannels. (a) $S_{e,}$ electron impact ionization source (cm^{-3} s^{-1}, 3-decade log scale). (b) [e], electron density (cm^{-3}, 3-decade log scale).(c) *E*/*N*,reduced electric field (Td, linear scale). The maximum value or range of values are indicated.

behavior and convex up water produces additional electric field enhancement at the leading edge of the water channels.

As with the dry channels, the bulk IW propagates into the empty channels directly under the jet. As the SIW begins to propagate along the surface, its trajectory is initially onto the surface of the water (channels 2, 3 and 4) due to the locally larger electric field at the surface of the water. Due to the short duration of the plasma-liquid interaction which is less than the dielectric relaxation time, the surface of the liquid charges negatively. This negative charging aids in launching a bulk IW towards the next channel. The IW is directed towards the electric field enhancement at the surface of the water in the next channel. As the water begins to protrude out of the channel to form a positive meniscus (channels 5–8), the electric field enhancement increases. For example, prior to the IW arriving at the water filling channel 3, the electric field at the surface of the water is 115 Td (28 kV cm^{-1}). Prior to the IW arriving at the water filling channel 5, the electric field at the leading edge of the water exceeds 250 Td (61 kV cm^{-1}). This increasingly large electric field enhancement then directs the IW from leading edge of the water in one channel to the leading of the water in the following channel. There is little contact of the IW wave with the solid dielectric surfaces of the ridges of the channels. This mode of plasma propagation is probably better described as a hopping bulk IW rather than a SIW.

Enlargements of the ionization source and electron density centered on the water filled channel 6 are shown in figure 14. The images begin with the IW having terminated on the leading edge of the water in the middle channel where electric field enhancement is the largest (9.5 ns). An electron density of 5 × 10^{14} cm^{-3} charges the leading edge of the water, which launches a negative IW (indicated by negative space charge in its ionization front) across the remainder of the water. The IW is directed towards the leading edge of the next water filled channel (9.9 ns). The negative IW closes the gap between leading edges with a plasma density of 5 × 10^{12} cm^{-3} (10.0 ns). With this being a negative IW, there is small density of electrons leading the IW, which seeds electrons in the region of electric field enhancement at the leading edge of the water in the next channel (9.9 ns, 10.0 ns). The seeding of electrons in the large *E*/*N* launches a positive IW back towards the prior water channel, indicated by positive space charge at the ionization front of the IW (10.2 ns). The termination of the positive IW on the leading edge of the water in the prior channel produces an electron density of 5 × 10^{14} cm^{-3} bridging the two leading edges (10.4 ns). The majority of the ionization in the bridge is produced by the reverse positive IW. This hopping IW leaves the majority of the both the water and the dielectric ridges not directly covered by plasma with arches of non-ionized gas between.

Validation of the trends for hopping IWs across the water-filled channels comes from comparison of the results of the simulations with ICCD imaging, shown in figure 15. The voltage in the simulations is −18 kV. The ICCD imaging shows filling of the dry channels with plasma directly under the jet. As the plasma propagates the bulk IWs first intersect

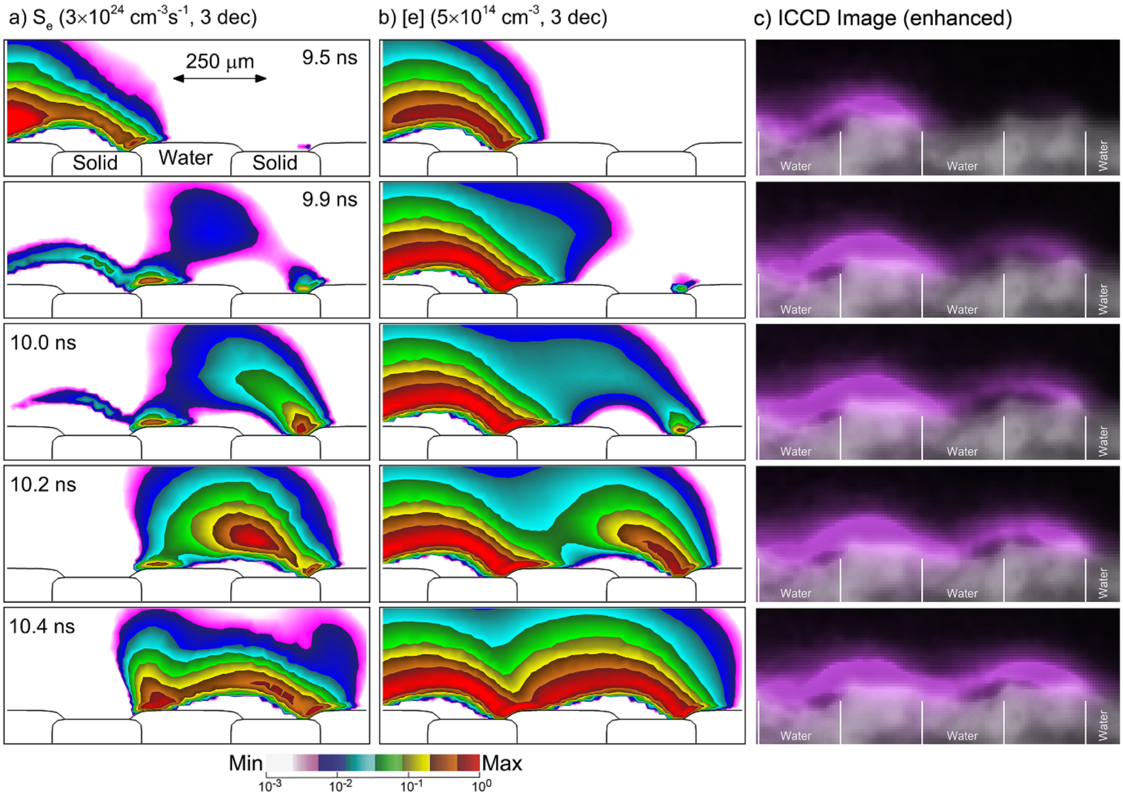

Figure 14. Plasma properties centered on water filled channel 6. Simulated (a) electron impact ionization source and (b) electron density. The time for the horizontally aligned images are indicated in the first column. The properties are shown in a 3-decade log scale with maximum value indicated. (c) ICCD images chosen at times to align with the simulations. The ICCD images have been enhanced to show dim detail. The boundaries between the water filled channels and ridges are indicated.

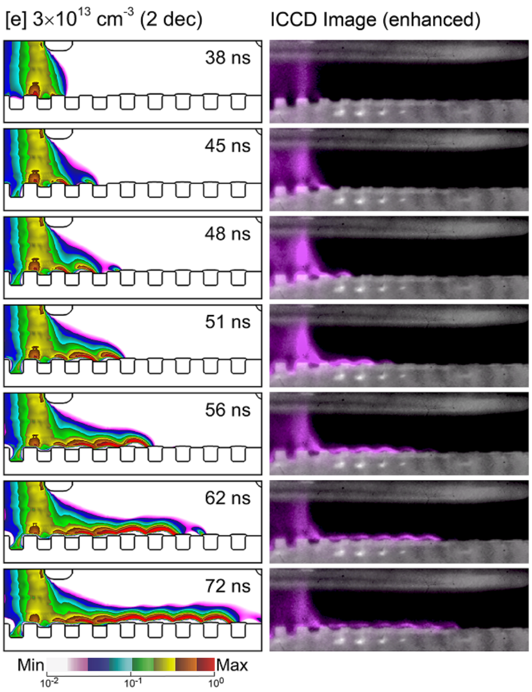

Figure 15. Comparison of (left) simulated electron density for applied voltage of −18 kV and (right) ICCD imaging for the Ar plasma jet propagating over water filled microchannels. The ICCD images have been enhanced to show dim detail, the electron density is plotted on a 2-decade log scale.

with the ridges of the channels where the channels contain little water. As the channels progressively fill with water, the IWs first intersect the middle of the water channel. As the IW wave propagates further along the chain, the IW intersects the leading edge of the fully water filled channels. This represents the transition from a SIW to the hopping IW mode from leading edge to leading edge of the water filled channels. These hops then leave regions of at best weakly ionized plasma, indicated by dark regions under the semicircular arches of hopping IWs.

The ICCD images also show the propagation of reverse IWs, as shown in figure 14. The sequence of the ICCD images was chosen to coincide with the timings of the simulations. The ICCD images indicate that the leading edge to leading edge gap is first closed by a forward IW. A reverse IW then propagates which produces a brighter image, indicating a higher plasma density. The trends shown by the simulations for the reverse IW closely align with the experimental imaging.

5. Concluding remarks

The use of APPs to treat non-planar, complex surfaces is challenged to uniformly treat those surfaces. For dielectric surfaces these challenges, in part, originate from electric field enhancement, polarization and charging of the surfaces which feed back to the plasma through, for example, higher rates of local ionization. The interaction of APPJs with the dielectric microchannels that might be found in labs-on-a-chip ultimately takes the form of a propagating sequence of SIWs and bulk IWs. Here we investigated negative APPJs sustained in Ar/N_2 mixtures propagating into ambient air and onto dry and water filled microchannels.

Propagation of the plasma across dry channels consists of SIWs across the top ridges followed by launching of bulk IWs across the channels directed towards the electric field enhancement at the vertex of the following ridge. Upon charging of that vertex, SIWs are launched across the ridge and into the interior of the preceding channel. The propagation of the plasma across the channels is then a sequence of bulk IWs which hop from across channels and SIWs which cover ridges and interiors of channels. This process leaves the trailing surfaces of the channel initially uncovered by plasma. The charging of the vertices of the microchannels produce backwards propagating positive IWs following the preionized path produced by the forward negative wave. Results from simulations are corroborated by experimental measurements of electric field using the EFISH technique and fast camera ICCD imaging.

The specifics of this pattern of hopping bulk IWs and SIWs depend on the permittivity and conductivity of the dielectric, but the general shape of the pattern remains. Materials with a high permittivity generally increase the total capacitance of the dielectric, which slows propagation of the SIW. However this observation is largely a consequence of the thickness of the dielectric being small compared to the electrode-surface gap. In cases where the dielectric is of comparable or larger thickness [11], the electric field in the gap increases with increasing permittivity, and the speed of the SIW may increase. Higher conductivity generally slows or stalls the SIW as conduction current is able to provide current continuity and negate the need for the expanding SIW to provide current continuity by displacement current.

The interaction of APPJs with water-filled channels was investigated for the conditions that were accessible in the experiments—empty to partially and fully water filled channels. The high electrical permittivity of water and the formation of a meniscus at the top of water filled channels produce triple point and polarization driven electric field enhancement. The transition between empty to fully filled water channels coincided with SIWs transitioning into hopping IWs. The hopping IWs propagate between the electric field enhanced leading edges of the water meniscus of each water filled channel. The majority of the ionization in arches of plasmas formed by the hopping result from backwards propagating, positive IWs. The hopping IW leaves large portions of both the dielectric and the water surfaces not directly exposed to plasma. These computed trends agree well with ICCD imaging.

Data availability statement

The data that support the findings of this study are contained in the paper and are available from the corresponding author upon reasonable request.

Acknowledgments

This work was supported by the Department of Energy Office of Fusion Energy Sciences (DE-SC0020232), the Army Research Office MURI program (W911NF-20-1-0105) and the National Science Foundation (CBET-2032604).

Conflict of interest

The authors have no conflicts of interest to disclose.

ORCID iDs

Kseniia Konina https://orcid.org/0000-0001-8933-1399
Sai Raskar https://orcid.org/0000-0003-4715-3146
Igor V Adamovich https://orcid.org/0000-0001-6311-3940
Mark J Kushner https://orcid.org/0000-0001-7437-8573

References

[1] Adamovich I *et al* 2022 *J. Phys. D: Appl. Phys.* **55** 373001
[2] Bogaerts A *et al* 2020 *J. Phys. D: Appl. Phys.* **53** 443001
[3] Chen Z, Koel B E and Sundaresan S 2022 *J. Phys. D: Appl. Phys.* **55** 055202
[4] Bolgeo T, Maconi A, Gardalini M, Gatti D, di Matteo R, Lapidari M, Longhitano Y, Savioli G, Piccioni A and Zanza C 2023 *J. Pers. Med.* **13** 736
[5] Hoffer P, Niedoba K, Jirásek V, Prukner V and Šimek M 2023 *Plasma Chem. Plasma Process.* **43** 1531–47
[6] Brandenburg R 2018 *Plasma Sources Sci. Technol.* **27** 079501
[7] Kettlitz M, Klink R, Höft H and Brandenburg R 2020 *Eur. Phys. J.* D **74** 110
[8] Winter J, Brandenburg R and Weltmann K D 2015 *Plasma Sources Sci. Technol.* **24** 064001
[9] Nijdam S, Teunissen J and Ebert U 2020 *Plasma Sources Sci. Technol.* **29** 103001
[10] Pechereau F, Bonaventura Z and Bourdon A 2016 *Plasma Sources Sci. Technol.* **25** 044004
[11] Marskar R and Meyer H K H 2023 *Plasma Sources Sci. Technol.* **32** 085010
[12] Hamdan A and Dorval A 2023 *J. Phys. D: Appl. Phys.* **56** 215202
[13] Zhang B, Sun Y, Han W, Fan L, Guo W, Li W, Mu H and Zhang G 2023 *Plasma Sources Sci. Technol.* **32** 075020
[14] Wang Q, Ning W, Dai D and Zhang Y 2020 *Plasma Process. Polym.* **17** 1900182
[15] Mujahid Z I, Kruszelnicki J, Hala A and Kushner M J 2020 *Chem. Eng. J.* **382** 123038
[16] Whitesides G M 2006 *Nature* **442** 368
[17] Shi H, Nie K, Dong B, Long M, Xu H and Liu Z 2019 *Chem. Eng. J.* **361** 635
[18] Chen F, Song J, Liu Z, Liu J, Zheng H, Huang S, Sun J, Xu W and Liu X 2016 *ACS Sustain. Chem. Eng.* **4** 6828
[19] Booth J P, Mozetič M, Nikiforov A and Oehr C 2022 *Plasma Sources Sci. Technol.* **31** 103001
[20] Wengler J, Ognier S, Zhang M, Levernier E, Guyon C, Ollivier C, Fensterbank L and Tatoulian M 2018 *React. Chem. Eng.* **3** 930
[21] Roszkowska P, Dickenson A, Higham J E, Easun T L, Walsh J L and Slater A G 2023 *Lab Chip* **23** 2720
[22] Ogunyinka O, Wright A, Bolognesi G, Iza F and Bandulasena H C H 2020 *Microfluid. Nanofluidics* **24** 13

[23] Patinglag L, Sawtell D, Iles A, Melling L M and Shaw K J 2019 *Plasma Chem. Plasma Process.* **39** 561
[24] Patinglag L, Melling L M, Whitehead K A, Sawtell D, Iles A and Shaw K J 2021 *Water Res.* **201** 117321
[25] Liu D, Zhang Y, Xu M, Chen H, Lu X and Ostrikov K 2020 *Plasma Process. Polym.* **17** e1900218
[26] Manríquez J J, Cataldo K, Vera-Kellet C and Harz-Fresno I 2014 *BMJ Clin. Evid.* **2014** 1711 (available at: www.ncbi.nlm.nih.gov/pmc/articles/PMC4278179/)
[27] Norberg S A, Johnsen E and Kushner M J 2015 *Plasma Sources Sci. Technol.* **24** 035026
[28] Scharfetter D L and Gummel H K 1969 *IEEE Trans. Electron Devices* **16** 64
[29] Lietz A M and Kushner M J 2016 *J. Phys. D: Appl. Phys.* **49** 425204
[30] Tian W, Tachibana K and Kushner M J 2014 *J. Phys. D: Appl. Phys.* **47** 055202
[31] Raskar S *et al* 2023 Spatio-temporal electric field distributions in an atmospheric plasma jet impinging on a microchannel array surface *Plasma Sources Sci. Technol.* submitted
[32] Lietz A M, Damany X, Robert E, Pouvesle J-M and Kushner M J 2019 *Plasma Sources Sci. Technol.* **28** 125009
[33] Höft H, Kettlitz M, Becker M M, Hoder T, Loffhagen D, Brandenburg R and Weltmann K-D 2014 *J. Phys. D: Appl. Phys.* **47** 465206
[34] Shao X J, Jiang N, Zhang G J and Cao Z X 2012 *Appl. Phys. Lett.* **101** 253509
[35] Keidar M 2015 *Plasma Sources Sci. Technol.* **24** 033001
[36] Norberg S A, Johnsen E and Kushner M J 2015 *J. Appl. Phys.* **118** 013301
[37] Morsell J, Bhatt N, Dechant C and Shannon S 2023 *J. Phys. D: Appl. Phys.* **56** 145201
[38] Joshi R P, Kolb J F, Xiao S and Schoenbach K H 2009 *Plasma Process. Polym.* **6** 763